Tunable narrow-band near-field thermal emitters based on resonant metamaterials

Jiayu Li, Baoan Liu, and Sheng Shen*

Department of Mechanical Engineering, Carnegie Mellon University, Pittsburgh, Pennsylvania 15213, USA

(Received 6 December 2016; revised manuscript received 28 May 2017; published 10 August 2017)

In the near field, Planck's law of blackbody radiation breaks down, and radiative heat transfer can be enhanced by orders of magnitude when surface polaritons are supported by interacting materials. However, such thermal radiation enhancement is strongly material dependent, thus difficult to control. Here, we propose a metamaterial-based structure consisting of patterned doped silicon nanorods that exhibits tunable narrow-band thermal emission. Direct numerical simulation based on the Wiener chaos expansion (WCE) method is performed to accurately investigate the heat transfer mechanism of metamaterials in the near field. The fundamental principle of the WCE method is elucidated, and an algorithm for symmetric and periodic structures is discussed. Implementation of the WCE method with the finite-difference time-domain method using the discrete dipole approximation (DDA) is also addressed in this paper.

DOI: 10.1103/PhysRevB.96.075413

I. INTRODUCTION

Near-field radiative heat transfer has attracted significant attention in recent years due to its wide potential in thermophotovoltaic (TPV) cells [1–3], thermal imaging [4–6], noncontact thermal rectifiers [7,8], thermal modulators [9–11], and thermal management [12–14]. In the near field, Planck's law of blackbody radiation breaks down, and radiative heat transfer can be greatly enhanced when the gap distance between objects is smaller than the dominant thermal wavelength predicted by Wien's displacement law [15–17]. It has been demonstrated that near-field radiative heat transfer can exceed the prediction from Planck's law by several orders of magnitude [18–20], especially when surface phonon polaritons (SPhPs) in polar dielectric materials (e.g., cubic boron nitride [cBN], SiC, or SiO_2) or surface plasmon polaritons (SPPs) in doped semiconductors are excited [18]. A number of groups have experimentally demonstrated that near-field radiation can exceed the blackbody limit using plate-plate or sphere-plate geometries [19–28].

Although near-field thermal radiation shows a dramatic heat transfer enhancement compared to far-field thermal radiation and is almost monochromatic in the infrared surface polariton resonance (IR-SPR) based materials, such thermal radiation enhancement and monochromatic thermal emission are strongly material-dependent. If the emitter and the absorber are made from different materials that support SPRs at different frequencies, the mismatch between SPR frequencies will result in much less heat transfer. To break this material restriction, broadband radiative thermal emitters and absorbers based on hyperbolic metamaterials are proposed to realize material-independent near-field enhancement [29,30]. In this paper, we propose a metamaterial-based structure consisting of patterned doped silicon nanorods that exhibits tunable narrow-band thermal emission. These metamaterial-based thermal emitters are extremely useful for TPVs and near-field thermal management.

In order to elucidate the heat transfer mechanisms of complex three-dimensional metamaterials, we directly calculate near-field radiation using the Wiener chaos expansion (WCE) formulation. For simple geometries, such as two parallel plates [31], parallel thin films [32], two spheres [33], sphere to plate [34], and infinitely long cylinders [35], where the analytical expression of dyadic Green's functions exists, thermal radiation can be directly calculated by evaluating the Maxwell equations analytically. However, for complex geometries, the aforementioned analytical approach is not feasible due to the lack of the analytical solution to the dyadic Green's functions. Therefore, highly efficient numerical methods are required to simulate the thermal radiation of arbitrary geometries. Some representative numerical methods for directly calculating thermal radiation are listed as follows: the scattering matrix method based on the rigorous coupled-wave analysis (RCWA) for periodic structures where the geometries are decomposed into multilayers [36,37]; the fluctuating surface current (FSC) method using the boundary element method where the geometric boundaries are decomposed into surface elements [38,39]; the Monte Carlo method by sampling thermally induced random currents [40]; the thermal discrete dipole approximation (T-DDA) method [41,42]; the near-field radiative transfer finite-difference time-domain (NF-RT-FDTD) method [43], which is a direct and nonstochastic algorithm accounting for the statistical nature of thermal radiation; and the fluctuating volume current (FVC) method [44]. The WCE method that we used in this paper is developed to calculate thermal radiation of arbitrary geometries by expanding thermally induced random currents onto deterministic orthonormal current modes [29,45,46]. Among the aforementioned methods, the RCWA method is very efficient for periodic layered structures with low to moderate index contrast. However, it becomes less efficient when applied to metal structures. The FSC method is essentially most efficient in terms of algorithm since it only requires surface meshing, yet it lacks the function of obtaining electromagnetic field profiles. Compared to other numerical methods for calculating near-field thermal radiation, the WCE method has the following advantages. First, in contrast to the formulations based on scattering theory, the WCE method does not require any mode expansion over the wave vector. It relies only on finding a proper set of orthonormal basis for a given geometry [29,46]. Thus, the WCE method can be used to calculate the thermal radiation from arbitrary geometries.

*Corresponding author: sshen1@cmu.edu

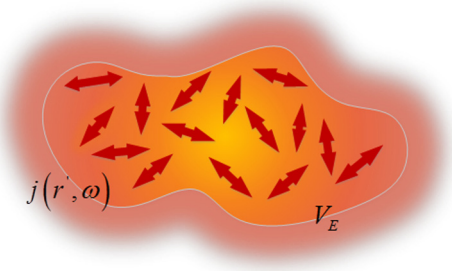

FIG. 1. Schematic of a radiative thermal emitter.

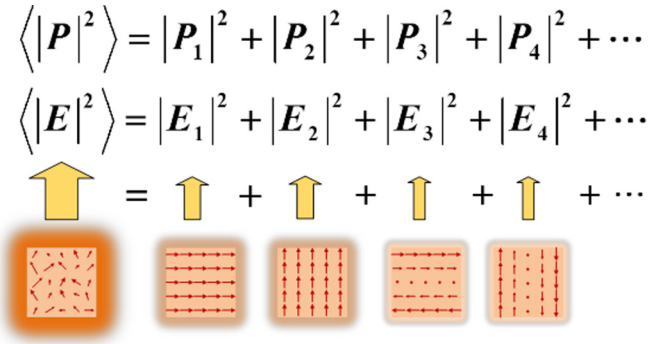

FIG. 2. Illustration of the concept of current mode expansion in the WCE method.

Second, the WCE method is a nonstochastic method and does not require any extra random number generators, whereas a proper random number generator is critical for the efficiency and accuracy of the Monte Carlo method. Furthermore, the WCE method can be implemented by the standard FDTD technique, which can obtain the spectral information (i.e., spectral energy flux from each mode) from a single simulation [29]. However, the data points at different frequencies need to be simulated by the frequency-domain methods, such as the FSC method and the finite-difference frequency-domain implementation of the WCE formulation [38,39]. Compared to previous papers regarding the WCE method [29,46], here we develop an algorithm to calculate the thermal radiation from symmetric and periodic structures. Furthermore, the implementation of the WCE formulation with the FDTD method is described by applying the DDA, which can be used in other numerical methods as well, such as the finite element method (FEM) and boundary element method (BEM).

II. PRINCIPLE OF THE WCE FORMULATION

According to fluctuational electrodynamics, thermal radiation originates from thermally induced random currents. Consider that a thermal emitter V_E at temperature T (as shown in Fig. 1), the field intensity $\langle|\boldsymbol{E}(r,\omega)^2|\rangle$, and the Poynting vector $\langle \boldsymbol{P}(r,\omega)\rangle_z$ can be expressed in terms of the dyadic Green's function and random currents $\boldsymbol{j}(r',\omega)$ as

$$\langle|\boldsymbol{E}(r,\omega)^2|\rangle = \omega^2\mu_0^2\Theta(\omega,T)\varepsilon_0 Im[\varepsilon]\int dr'^3\int dr''^3 \mathrm{Tr} \times [\boldsymbol{G}(r,r',\omega)^*\cdot\boldsymbol{G}(r,r'',\omega)\cdot\langle j(r'',\omega)j(r',\omega)\rangle], \tag{2.1}$$

$$\langle \boldsymbol{P}(r,\omega)\rangle_z = -i\omega\mu_0\varepsilon_0\int dr'^3\int dr''^3 \mathrm{Tr}[\boldsymbol{G}(r,r',\omega)_x{}^* \cdot \boldsymbol{G}^H(r,r'',\omega)_y\cdot\langle \boldsymbol{j}(r'',\omega)\boldsymbol{j}^*(r',\omega)\rangle]. \tag{2.2}$$

$\langle \boldsymbol{j}(r'',\omega)\boldsymbol{j}^*(r',\omega)\rangle$ equals a deterministic expression defined by the fluctuation-dissipation theorem.

The volume integral in the above equations is conducted in the volume of thermal emitters V_E; Tr[·] is the trace of the matrix, and we use the property of $\mathrm{Tr}[ABC] = \mathrm{Tr}[BCA]$. $\boldsymbol{G}^{\boldsymbol{H}}(r,r'',\omega)$ indicates the magnetic dyadic Green's function, which is defined as $H(r,\omega) = \int dr'\boldsymbol{G}^{\boldsymbol{H}}(r,r'',\omega)\cdot\boldsymbol{j}(r',\omega)$, and can be further expressed as $\boldsymbol{G}^{\boldsymbol{H}}(r,r'',\omega) = \mu_0\nabla_r\times\boldsymbol{G}(r,r',\omega)$, where $\langle\cdot\rangle$ denotes the statistical ensemble average.

The formulations based on fluctuational electrodynamics in Eqs. (2.1) and (2.2) provide the first-principles evaluation for thermal radiation. However, directly computing these two formulas turns out to be extremely difficult in general cases where geometries are complex.

In order to efficiently evaluate Eqs. (2.1) and (2.2), the WCE formulation is used to calculate thermal radiation of arbitrary geometries by expanding the thermally induced random current $\boldsymbol{j}(r',\omega)$ onto deterministic orthonormal current modes [29,46]. As a result, thermal radiative heat flux and field profile are obtained by the sum of the energy flux and the field emitted from each current mode, respectively, as illustrated in Fig. 2. By choosing the current mode in the multipole expansion form, the summation can be fast converging in practice. Consequently, only a few number of current modes are required to be numerically simulated, and thermal radiation can thus be calculated with high computational efficiency.

According to fluctuational electrodynamics in Eqs. (2.1)–(2.3), the heat flux $\langle P_z\rangle$ and the field profile $\langle|E|^2\rangle$ are determined by the first and the second moments of the random currents, i.e., $\boldsymbol{j}(r,\omega)$ and $\langle\boldsymbol{j}(r,\omega)\boldsymbol{j}^*(r',\omega)\rangle$, with the value of

$$\begin{aligned}\langle\boldsymbol{j}(r,\omega)\rangle &= 0,\\ \langle\boldsymbol{j}(r,\omega)\boldsymbol{j}^*(r',\omega)\rangle &= V_T(r,\omega)^2\delta(r-r')\boldsymbol{I},\end{aligned} \tag{2.3}$$

where $\langle\boldsymbol{j}(r,\omega)\rangle$ is attributed to the unbiased nature of the thermal fluctuation; $V_T(r,\omega) = \sqrt{\frac{4}{\pi}\omega\varepsilon_0\mathrm{Im}[\varepsilon(r)]\Theta(\omega,T)}$ is a deterministic quantity according to Eq. (2.3). Under the constraint of Eq. (2.3), the random current $\boldsymbol{j}(r,\omega)$ can be mathematically constructed as

$$\boldsymbol{j}(r,\omega) = V_T(r,\omega)dW_i(r)\hat{\boldsymbol{i}},\quad r\in V_E, i=x,y,z, \tag{2.4}$$

where dW_x, dW_y, and dW_z are the white-noise stochastic processes that have the properties of $\langle dW_l(r)\rangle = 0, \langle dW_l(r)\cdot dW_k(r')\rangle = \delta(r-r')$ for $r,r'\in V_E; l,k\in\{x,y,z\}$.

In addition, dW_x, dW_y, and dW_z are independent of each other, i.e., $\langle dW_l(r)\cdot dW_k(r')\rangle = \langle dW_l(r)\cdot dW_k(r)\rangle = 0$ for $l\neq k; l,k\in\{x,y,z\}$, indicating that the random polarization of the random current $\langle\boldsymbol{j}(r,\omega)\rangle$. Such a stochastic process can be expanded onto a deterministic orthonormal basis by the

WCE method as [46]

$$dW_m(r) = \sum_{n=1}^{\infty} c_{mn} \cdot f_n(r), r \in V_E, \quad m = x,y,z, \tag{2.5}$$

where c_{mn} are the uncorrelated random variables satisfying $\langle c_{ml} \rangle \langle c_{ml} \cdot c_{mk} \rangle = \delta_{lk} \cdot \{f_n(r)\}$. $\{f_n(r)\}$ is a set of orthonormal basis functions defined in the volume of the thermal emitter V_E. An arbitrary function $H(r)$ can be used to describe a random process as

$$H(r) = \sum_{n=1}^{\infty} a_{mn} \cdot f_n(r)\hat{\boldsymbol{m}}, m = x,y,z, \tag{2.6}$$

where the coefficients $\{a_{mn}\}$ are random variables for a specific polarization direction,$\{f_n(r)\}$ can be chosen in an arbitrary form as long as the completeness and orthonormality are satisfied. For instance, $\{f_n(r)\}$ can have the form of Fourier series if the shape of the thermal emitter is a rectangular prism. $\{f_n(r)\}$ can even be the Dirac delta function, i.e., $\{f_i(r)\} = \delta(r - r_i), \forall r_i \in V_E$, in which the WCE formulation turns into the brute force method. By substituting Eq. (2.5) into Eq. (2.4), the thermally induced random current $\boldsymbol{j}(r,\omega)$ can be expressed in terms of the orthonormal basis functions $\{f_n(r)\}$ as

$$\boldsymbol{j}(r,\omega) = \sum_m \sum_n c_{mn} \cdot [V_T(r,\omega) f_n(r)]\hat{\boldsymbol{m}}, \quad r \in V_E, m = x,y,z, \tag{2.7}$$

where c_{xn}, c_{yn}, and c_{zn} are the random variables satisfying $\langle c_{ki} \rangle = 0, \langle c_{ki} \cdot c_{mj} \rangle = 1$ for $i = j, k = m$, and $\langle c_{ki} \cdot c_{mj} \rangle = 0$ otherwise.

Therefore, the second moment of random current $\langle \boldsymbol{j}(r,\omega)\boldsymbol{j}^*(r',\omega) \rangle$ in Eq. (2.3) can be readily expressed as

$$\langle \boldsymbol{j}(r,\omega)\boldsymbol{j}^*(r',\omega) \rangle = \sum\nolimits_n V_T^2 f_n(r) f_n(r')\boldsymbol{I}. \tag{2.8}$$

Substituting Eq. (2.8) into Eq. (2.2), the radiative heat flux equals

$$\langle \boldsymbol{P}(r,\omega) \rangle_z = \int dr'^3 \int dr''^3 \mathrm{Tr} \times \left[\boldsymbol{G}\boldsymbol{G}_{\boldsymbol{P}} \cdot \left(\left(\sum_i V_T^2 f_i(r') f_i(r'') \right) \right) \cdot \boldsymbol{I} \right], \tag{2.9}$$

where we simplify the dyadic Green's function term $-i\omega\mu_0[\boldsymbol{G}(r,r',\omega)_x^* \cdot \boldsymbol{G}^{\boldsymbol{H}}(r,r'',\omega)_y]$ as $\boldsymbol{G}\boldsymbol{G}_{\boldsymbol{P}}(r,r',r'',\omega)$, or $\boldsymbol{G}\boldsymbol{G}_{\boldsymbol{P}}$. We also denote the operator $\boldsymbol{L}_{\boldsymbol{P}}[\cdot]$ as $\boldsymbol{L}_{\boldsymbol{P}}[\boldsymbol{X}(r',r'',\omega)] = \int dr'^3 \int dr''^3 \mathrm{Tr}[\boldsymbol{G}\boldsymbol{G}_{\boldsymbol{P}} \cdot \boldsymbol{X}(r',r'',\omega)]$, and $\boldsymbol{L}_{\boldsymbol{P}}[\cdot]$ is a linear operator [29]. Recall that three independent polarizations of current density are $j_{n,i}(r,\omega) = V_T(r,\omega) f_n(r)\boldsymbol{i}, i = x,y,z$. Then, Eq. (2.9) can be represented as

$$\langle \boldsymbol{P}(r,\omega) \rangle_z = \sum_n P_n = \sum_n \{\boldsymbol{L}_{\boldsymbol{P}}[\boldsymbol{j}_{n,i} \cdot \boldsymbol{j}^*{}_{n,i}]\}, \; i = x,y,z. \tag{2.10}$$

In Eq. (2.10), $\boldsymbol{L}_{\boldsymbol{P}}[\boldsymbol{j}(r',\omega) \cdot \boldsymbol{j}^*(r'',\omega)]$ physically indicates the energy flux due to a given current density distribution $\boldsymbol{j}(r',\omega)$.

Similarly, the thermal radiation field intensity $\langle |\boldsymbol{E}(r,\omega)^2| \rangle$ can be expanded in terms of current modes based on the aforementioned derivation as

$$\langle |\boldsymbol{E}(r,\omega)^2| \rangle = \sum_n \left| E_n^2 \right| = \sum_n \{\boldsymbol{L}_{\boldsymbol{E}}[\boldsymbol{j}_{n,i} \cdot \boldsymbol{j}^*{}_{n,i}]\}, i = x,y,z, \tag{2.11}$$

where the operator $\boldsymbol{L}_{\boldsymbol{E}}[\cdot]$ is defined as $\boldsymbol{L}_{\boldsymbol{E}}[X] = \omega^2\mu_0^2 \int dr'^3 \int dr''^3 \mathrm{Tr}[\boldsymbol{G}(r,r',\omega)^* \cdot \boldsymbol{G}(r,r'',\omega) \cdot \boldsymbol{X}]$.

The concept of current modes expansion depicted in Eqs. (2.10) and (2.11) is further illustrated in Fig. 2. The energy flux and the field intensity from each current mode can be easily calculated by setting up the electric current source accordingly.

III. THE WCE FORMULATION FOR PERIODIC AND SYMMETRIC GEOMETRIES

There still exist two major challenges for the WCE formulation. One challenge is to select a proper volume for random current expansion; the other is to find proper current modes of thermal emitters within a certain expansion volume in order to achieve fast convergence. Regarding the first challenge, be very cautious to choose a proper volume as the large volume expansion will severely deteriorate the efficiency of element decomposition in the WCE formulation [47,48]. Since we are usually interested in large-scale geometric structures, especially the structures with symmetry and periodicity in certain dimensions, developing a methodology to efficiently implement the WCE formulation in infinite and periodic structures is extremely important and useful.

In the present paper, we develop a formalism to choose proper current modes by taking advantage of the symmetry and periodicity of the geometries, leading to a high computational efficiency in large and periodic structures. In this scenario, we consider a periodic structure composed of a thin film absorber V_A and a grating emitter V_E, as shown in Fig. 3. Rather than finding the current modes directly for the whole volume of the emitter V_E, we expand the current modes only for a unit cell of the emitter, where the unit cell is the smallest repeating unit in the emitter based on the periodicity and symmetry of the whole structure. In Fig. 3, by translating the unit cell $V_{c,n}$, the entire emitter $\sum V_{c,n}$ can be replicated. Note that the orthonormal basis functions $\{f_n(r)\}$ in this scenario only require to be defined inside a single unit cell, i.e., $r \in V_{c,n}$, because the basis functions in all the unit cells are essentially the same, i.e., $\{f_n(r + pm)\}$ with the translation of the coordinates. As a result, the set of the basis functions from all unit cells satisfies the orthonormality and completeness for the whole volume of the emitter $\sum V_{c,n}$.

In order to justify that the expansion of current modes in a unit cell is sufficient for the calculation of overall heat flux from the entire emitter to the entire absorber, we utilize the unique property of Green's function for periodic and symmetric structures at thermal equilibrium, namely $G(r,r',\omega) \equiv G(R,\omega)$, where $R = r - r'$, r is the electromagnetic field spatial location, r' is the spatial location of the source point, and R is the relative position between field and source point locations. Consequently, the Poynting vector $P(r,r',\omega)$ and the

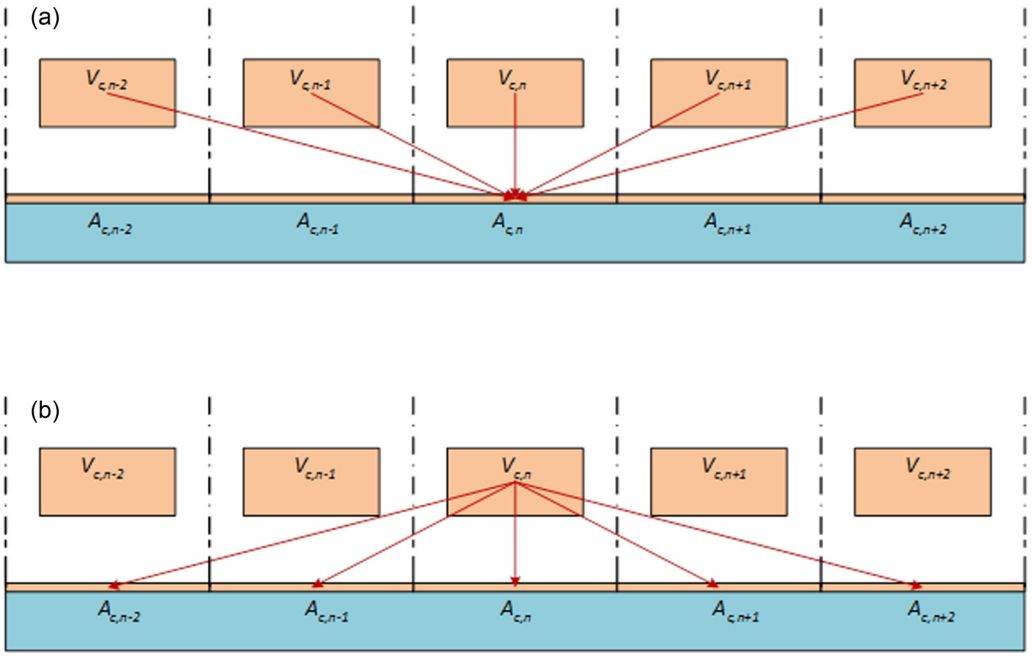

FIG. 3. Schematics of a periodic and symmetric structure composed of a thin film absorber $\sum A_{c,n}$ and a grating emitter $\sum V_{c,n}$ with the heat fluxes (a) from the entire emitter volume to single absorber unit cell surface area $A_{c,n}$ and (b) from single emitter unit cell volume to the entire absorber surface area.

resulting heat flux $q(r,r',\omega)$ are only the functions of relative spatial position of source and field points [38], according to Eqs. (2.2) and (2.3). We start from investigating the overall heat flux Q that a single unit cell surface area $A_{c,m}$ on the absorber receives from the entire emitter $\sum V_{c,n}$, as shown in Fig. 3(a),

$$Q(A_{c,m}) = \sum_n q_{nm}\left(r_{A_{c,m}}, r'_{V_{c,n}}, \omega\right), \tag{3.1}$$

where $q_{nm}(r_{A_{c,m}}, r'_{V_{c,n}}, \omega)$ denotes the heat flux from the unit emitter cell $V_{c,n}$ to the unit absorber cell surface area $A_{c,m}$. Then we calculate the heat flux that a single unit cell of the emitter contributes to the entire absorber surface area $\sum A_{c,n}$, as shown in Fig. 3(a),

$$Q(V_{c,m}) = \sum_n q_{mn}\left(r_{A_{c,n}}, r'_{V_{c,m}}, \omega\right). \tag{3.2}$$

From Eqs. (3.1) and (3.2), $\sum_n q_{nm}(r_{A_{c,m}}, r'_{V_{c,n}}, \omega)$ is equal to $\sum_n q_{mn}(r_{A_{c,n}}, r'_{V_{c,m}}, \omega)$. Therefore, the radiative heat flux between the emitter $\sum V_{c,n}$ and the absorber $\sum A_{c,n}$ can be obtained by calculating the energy fluxes due to a single unit cell volume. Since the size of the unit cell $V_{c,n}$ is much smaller than the size of the emitter $\sum V_{c,n}$, the current mode expansion in a single unit cell leads to a faster convergence speed in comparison with directly expanding the current modes in the entire emitter volume, making the WCE formulation computationally efficient for the periodic and symmetric structures.

With regard to the second challenge of finding proper current modes of thermal emitters, it can be solved by introducing the dipole expansion. For instance, when the current modes are chosen in sinusoidal forms, their expansion can be physically viewed as a classical multipole expansion, which leads to fast convergence for energy flux calculation. Hence, we can truncate the expansion and keep the only lower order current modes without losing accuracy. For an emitter with a rectangular prism shape, defined in the Cartesian coordinates as $x \in [0,a], y \in [0,b], z \in [0,c]$, the current modes can be chosen in the form of Fourier series as $\boldsymbol{j}_{l,m,n}(r,\omega) = V_T \cdot [H_l(x)P_m(y)Q_n(z)]\{\hat{\boldsymbol{x}},\hat{\boldsymbol{y}},\hat{\boldsymbol{z}}\}$, where the fundamental mode is $\boldsymbol{j}_{0,0,0}(r,\omega) = V_T \cdot \frac{1}{\sqrt{abc}}\{\hat{\boldsymbol{x}},\hat{\boldsymbol{y}},\hat{\boldsymbol{z}}\}$, and $H_l(x) = \sqrt{\frac{2}{a}}\cos[\frac{l\pi x}{a}], l = 1,2,3,\ P_m(y) = \sqrt{\frac{2}{b}}\cos[\frac{m\pi y}{b}], m = 1,2,3,\ Q_n(z) = \sqrt{\frac{2}{c}}\cos[\frac{n\pi z}{c}], n = 1,2,3$ for the higher order modes. For complicated geometries, while some special algorithms can be used to generate the current modes in spherical harmonic forms [49], an alternative method is to first decompose the complicated geometries into a certain number of regular ones, then define the corresponding number of the piecewise volume current density function and sum up their contributions, where each of these functions is nonzero only in one decomposed geometry region.

One example is the near-field thermal radiation between two SiC thin films (as shown in Fig. 4). These two thin films have thicknesses of $L_1 = 1\ \mu$m and $L_2 = 5\ \mu$m, respectively, and the gap between them is 100 nm. Since the structure is uniform in both the x and the y directions, it is essentially a periodic structure. In this case, there are two choices for unit cell. The more intuitive one is the unit cell with the geometric shape of a cuboid: $x \in [x_c, x_c + L_x] \cup y \in [y_c, y_c + L_y] \cup z \in [0, L_z]$, while the other choice is the optimal one by choosing a straight line, i.e., $x \in [x_c, x_c + \Delta x] \cup y \in [y_c, y_c + \Delta y] \cup z \in [0, L_z]$, for any x_c, y_c where $\Delta x \ll L_z, \Delta y \ll L_z$. The WCE current mode expansions in both of the unit cells render the same radiative thermal heat fluxes, yet the convergence or computation speed can be significantly increased in the

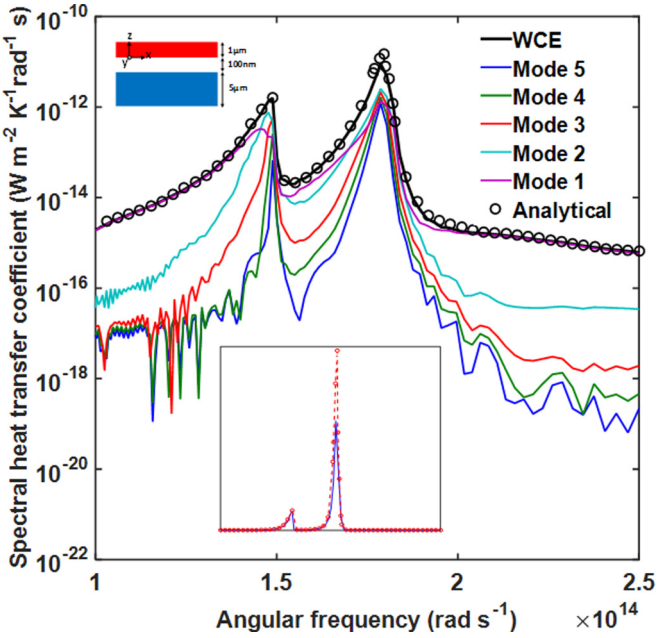

FIG. 4. Spectral heat flux between two thin SiC films calculated by the WCE method. Inset: the comparison of WCE and analytical results [50–52] plotted in the linear scale, where the red circles represent the analytical results and the blue curve represents the WCE results.

straight-line case. Figure 4 plots the simulated spectral heat flux at the temperature of 300 K with the contribution from each current mode. The temperature of the absorber is set as 0 K. The first four current modes $m_1, \ldots, m_4$ corresponding to the induced current density $\boldsymbol{j}_{0,0,0}, \cdots \boldsymbol{j}_{0,0,3}$ in the unit cell volume are expanded, namely $\boldsymbol{j}_{0,0,0}(r,\omega) = V_T \frac{1}{\sqrt{abc}}\hat{\boldsymbol{z}}$, $\boldsymbol{j}_{0,0,1}(r,\omega) = V_T\sqrt{\frac{2}{L_z}}\cos[\frac{\pi z}{L_z}]\hat{\boldsymbol{z}}$, $\boldsymbol{j}_{0,0,2}(r,\omega) = V_T\sqrt{\frac{2}{L_z}}\cos[\frac{2\pi z}{L_z}]\hat{\boldsymbol{z}}$, $\boldsymbol{j}_{0,0,3}(r,\omega) = V_T\sqrt{\frac{2}{L_z}}\cos[\frac{3\pi z}{L_z}]\hat{\boldsymbol{z}}$, where $V_T(r,\omega) = \sqrt{\frac{4}{\pi}\omega\varepsilon_0 Im[\varepsilon(r)]\Theta(\omega,T)}$. For each current mode, the energy flux emitted from it to the xy plane in the gap is recorded. The heat flux between two thin films is calculated as the sum of the energy flux due to each mode and is then normalized to the lateral area of the unit cell, i.e., $S = L_x L_y$. A faster convergence speed of the current mode expansion is observed in the calculation using a straight-line unit cell, as the contributions from the third and the fourth modes are almost the same and both orders of magnitude are less than that from the first mode. The result from the WCE formulation agrees well with the analytical result in Refs. [50–52], which convincingly validates our formalism.

The main technical challenge in the implementation of the WCE formulation using the finite element method is the setup of the continuous current modes by using discrete point dipole sources. In fact, discrete point dipoles are the only choice in the main stream of simulation methods as continuous current density modes are not supported by most simulation software. Moreover, discrete dipole approximation can be used to mimic any current density modes. Figure 5 illustrates the setup of a continuous volume current density. Consider a continuous current distribution $\boldsymbol{j}(x) = f(x)\hat{\boldsymbol{z}}$ along a straight line

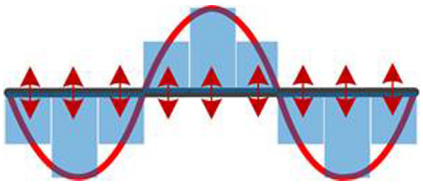

FIG. 5. Discrete dipole approximation to a continuous current density.

$x \in [0,L]$, which is illustrated as the red curve in Fig. 5. We first approximate it as a step function $F(x)\hat{\boldsymbol{z}}$ illustrated as the blue histogram. Assuming that the width of each step is ΔL_x, the step function can be expressed as

$$F(x) = \sum_n f(x_n)\left[u\left(x - \left(x_n - \frac{\Delta L_x}{2}\right)\right) - u\left(x - \left(x_n + \frac{\Delta L_x}{2}\right)\right)\right], \tag{3.3}$$

where $\{x_n\}$ indicates the center point of each step, i.e., $x_n = n \cdot \Delta L_x - \frac{\Delta L_x}{2}$, $u(x)$ is a step function, with $u(x) = 1$ for $x \geqslant 0$ and $u(x) = 0$ for $x < 0$. Equation (3.3) can be further expressed as

$$F(x) \approx \sum_n f(x_n)(\delta(x - x_n)\Delta L_x), \tag{3.4}$$

given that $\delta(x - x_n) = \frac{\partial u(x-x_n)}{\partial x} \approx [u(x - (x_n - \frac{\Delta L_x}{2})) - u(x - (x_n + \frac{\Delta L_x}{2}))]/\Delta L_x$. Equation (3.4) indicates that the current density $F(x)\hat{\boldsymbol{z}}$ can be mimicked by the point dipole sources located at $\{x_n\}$. The actual three-dimensional current density can thus be easily set up by multiplying the other two-dimensional current density as $F(r) = \sum_n f(x_n,y_n,z_n)\prod_{i=x,y,z}[u(i - (i_n - \frac{\Delta L_i}{2})) - u(i - (i_n + \frac{\Delta L_i}{2}))]$. Applying the step function approximation again, the actual three-dimensional current density then becomes

$$F(r) \approx \sum\nolimits_n f(x_n,y_n,z_n)V_c \prod\nolimits_{i=x,y,z} \delta(i - i_n). \tag{3.5}$$

The dipole moment is $p_n = f(r)V_c$, where $V_c = \Delta L_x \times \Delta L_y \times \Delta L_z$ is the cell volume in the finite element software. Then the actual thermally induced volume current density can be calculated by the WCE formulation with the implementation of DDA.

IV. NEAR-FIELD THERMAL EMISSION FROM RESONANT METAMATERIALS

Here we design a metamaterial-based structure with a layer of patterned nanorod thermal emitters that shows the potential of tuning resonant near-field radiation. We use the WCE formulation to investigate the near-field radiative heat transfer in two cases: The first case is an array of infinitely long nanorod emitters over a thin film [Fig. 6(a)]; the second case is a layer of patterned finite size nanorod emitters over a thin film [Fig. 6(b)]. Both the structures in our simulation are considered to be infinitely large in the lateral direction. The cross section of nanorods has a square shape with a fixed length of 200 nm. The material used for the whole structure

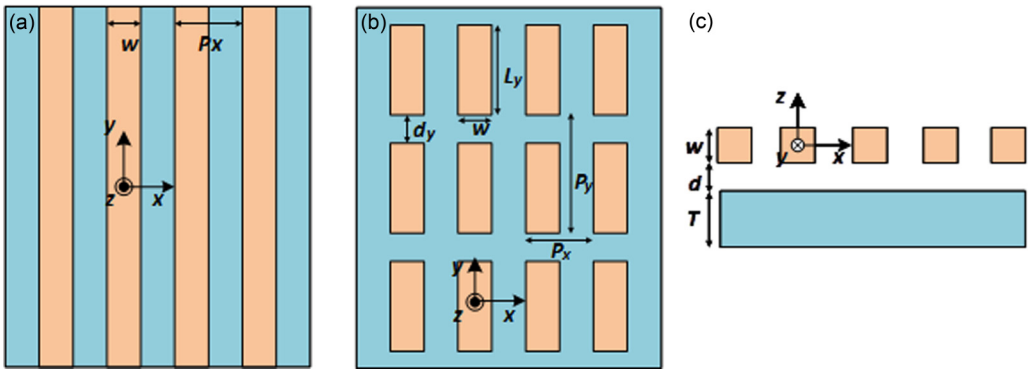

FIG. 6. (a) Schematic of an array of infinitely long nanorod emitters over a thin film, where $w = 200\,\text{nm}$; (b) schematic of a layer of patterned finite size nanorod emitters over a thin film, where $w = 200\,\text{nm}, d = 100\,\text{nm}, T = 400\,\text{nm}$, L_y is the length of the finite size nanorod emitter, P_x is the periodicity in the x direction, P_y is the periodicity in the y direction, and d_y is the distance between two nanorod emitters in the y direction and fixed to be 1 μm; and (c) schematic of the cross section in (b).

is arsenic doped n-type silicon with doping concentration of $5 \times 10^{21}\,\text{cm}^{-3}$ [53]. The nanorod emitter is kept at 300 K, while the thin film layer is maintained at 0 K as an absorber. The heat flux between them is evaluated by calculating the amount of energy transmitted into the thin film layer. As the thin film layer is at a finite temperature, the net heat flux can be solved by the reciprocity of radiative heat transfer. In our simulation, the current modes in the nanorod emitters are chosen in sinusoidal forms because of the resulting high convergence speed of numerical simulation. The thin film layer at 0 K does not emit thermal radiation, and we only consider their electromagnetic response in the infrared range. In this interested frequency range, the n-type silicon always has a negative real part of its permittivity, which indicates that doped silicon behaves like metal but does not have intrinsic plasmon polariton frequency.

We first study the radiative heat transfer between an array of infinitely long nanorods and a thin film with a fixed gap distance of 100 nm. The spectral heat flux between the nanorod emitters and the thin film absorber at different period P_x is plotted in Fig. 7. In Fig. 7(c), the unit cell for the WCE current mode expansion is chosen as a cuboid within the nanorod, which is placed at the middle point of the simulation region. It should be noted that only half of the cuboid within the nanorod, as denoted in orange, needs discrete point dipole expansion due to the symmetry of the structure along the x direction. The WCE current mode basis function is chosen as sinusoidal forms described in Sec. III. First, five current modes are expanded in the unit cell to calculate the near-field thermal radiation. The heat flux spectra for the structures in Figs. 7(b) and 7(c) behave like straight lines at frequencies ranging from 0.5×10^{14} to $5 \times 10^{14}\,\text{rad/s}$, which shows that there is no intrinsic resonance frequency for the n-type silicon. Decreasing the period P_x between adjacent infinitely long nanorods, the overall heat flux spectrum between the nanorod emitters and the thin film absorber increases accordingly. This negative correlation between spectral heat flux intensity and nanorod emitter period P_x is because increasing the period reduces the effective thermal emitters' volume per unit area. It should be noted that the increasing trend of spectral heat flux with decreasing angular frequency is due to the large local density of states (LDOS) in the long wavelength range for the heavily doped silicon [54,55].

In Fig. 8(a), consider an array of finite size nanorods as thermal emitters periodically aligned over a thin film absorber, where the cross section of one nanorod is still a 200 nm $\times$ 200 nm square. The gap between the nanorod emitters and the thin film absorber is set to be 500 nm. The near-field radiative heat flux is normalized to the area of the smallest repeating unit cell of the structure. Here, only a quarter of one nanorod thermal emitter is chosen as the WCE unit cell due to the symmetry in both the x and the y directions. The spectral heat flux between the periodically aligned nanorod emitters and the thin film absorber is plotted in Fig. 8(b). The green and the red curves are the heat flux spectra for the cases of finite-size nanorod emitters with different lengths in the y direction. The blue curve is the heat flux spectra for the case of infinitely long nanorod emitters. We can clearly see from Figs. 8(b) and 8(d) that there are multiple near-field heat flux peaks. At each peak

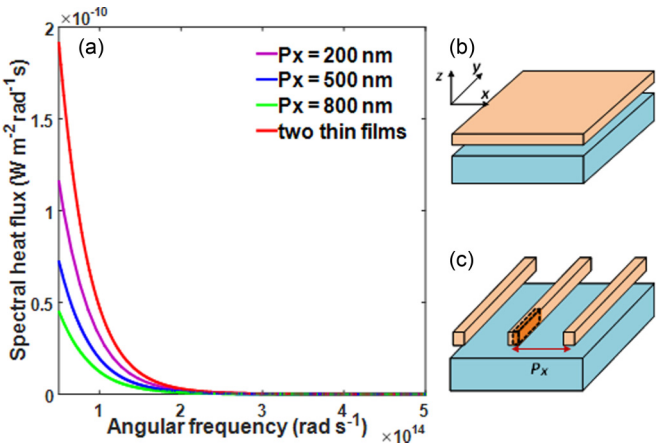

FIG. 7. Radiative thermal heat fluxes from the structures of infinitely long nanorods over thin film in comparison with the case of two thin films. (a) Radiative heat fluxes normalized to the effective surface area; (b) schematic of the structure of two thin films at the gap distance of 100 nm; and (c) schematic of the structure with a layer of patterned infinitely long nanorods emitters over a thin film. The orange region with a dashed line contour is the WCE unit cell.

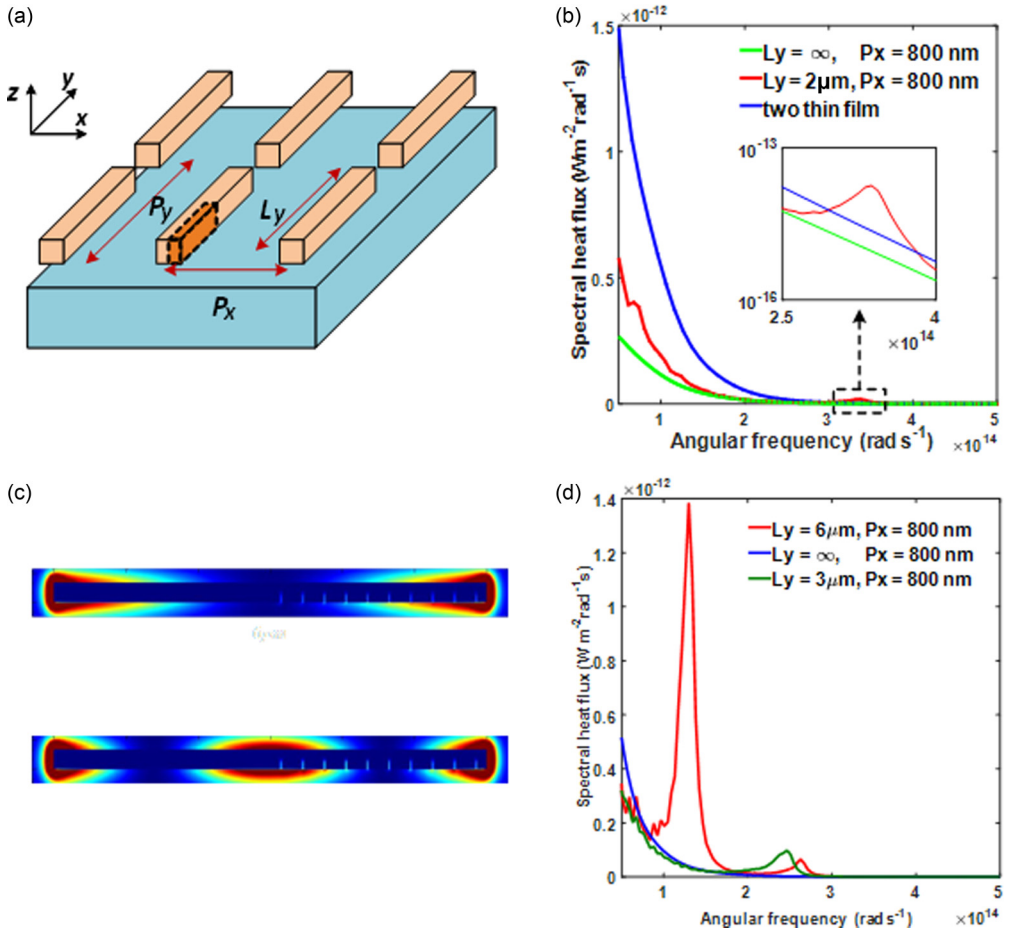

FIG. 8. Radiative thermal heat fluxes from the structures of finite size nanorods over a thin film in comparison with the case of two thin films. (a) Schematic for the structures, where P_x and P_y are the period along the x and the y directions, respectively. The gap distance between the two layers is 500 nm, and the cuboid marked in orange is the WCE unit cell, which is a quarter of single nanorod. (b) Spectral heat fluxes for the cases of the thin film emitter (blue curve), the nanorod thermal emitter with $L_y = 2\ \mu$m (red curve), and the infinitely long nanorod thermal emitter (green curve). (c) Electric field profiles $|\boldsymbol{E}|^2$ of the first and second modes for the single nanorod resonator (6 μm in length), where 10 small bright lines in the right part of the nanorod are the discrete dipole sources. (d) Spectral heat fluxes between the structures with different nanorod periods in the y direction.

point, the heat flux intensity is at least one order of magnitude larger than the case of infinitely long nanorod emitters and can be larger than the case of two thin films, even though the overall thermal emitter volume is decreased.

The mechanism for this nonintrinsic near-field enhancement can be elucidated by the transmission line waveguiding mode or Fabry-Pérot cavity effect [56], which greatly increases the mode number per unit emitter area. Transmission lines are essentially the waveguides composed of one or multiple metallic wires, which can efficiently guide the terahertz and infrared waves with highly confined waveguiding modes. We use the WCE formulation based on the FDTD method to directly calculate the electric field profile of one transmission line resonator in the structure [as shown in Fig. 8(a)]. In Fig. 8(c), the intensity profile of the electrical field $|\boldsymbol{E}|^2$ is plotted for the first mode and the second mode of the transmission line resonator. Figure 8(c) clearly shows that the resonant modes of the transmission line resonator are essentially the Fabry-Pérot type resonance of the waves along the nanorod, where the fundamental resonant wavelength $\lambda = 2L_y \times Re[n_g]$ and n_g is the effective index of the corresponding waveguide mode. By truncating one infinitely long nanorod emitter into small finite-size nanorod emitters, transmission line modes are introduced to each small nanorod emitter, especially at the resonant frequency, and eventually these extra modes make their contributions to the overall heat flux. The fundamental mode corresponds to the smallest peak frequency $\omega_0 = \frac{\pi c}{L_y Re[n_g]}$, where c is the speed of light in the vacuum, L_y is the length of single finite-size nanorod in the y direction, and n_g is the propagating index of the waveguide. As shown in Fig. 8(d), the heat flux spectrum corresponding to different values of P_y is plotted (where $P_y = L_y + d_y$, d_y is the gap distance between two adjacent nanorods in the y direction and is fixed to be 1 μm for all the cases). The first spectral heat flux peak in the red curve corresponding to 6 μm long nanorod emitters is centered around $\omega_0 = 1.34 \times 10^{14}$ rad/s given that $Re[n_g] \approx 1.18$ for the first mode. Similarly, the spectral heat flux of 3 μm long nanorod emitters (blue curve) has a peak around $\omega_0 = 2.5 \times 10^{14}$ rad/s given that $Re[n_g] \approx 1.16$. The other larger peak frequency ω for the finite-size

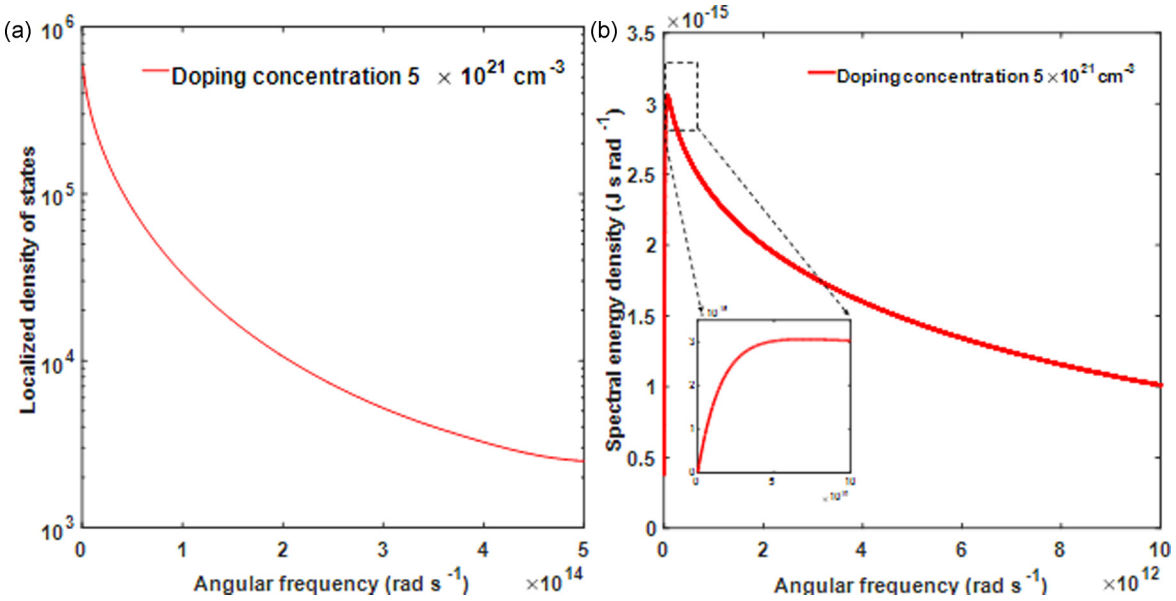

FIG. 9. (a) Localized density of states (red curve) at a distance of 100 nm from the surface of a 400 nm thick doped silicon film with doping concentration of 5×10^{21} cm^{-3}. (b) Spectral energy density plot at a distance of 100 nm from the surface of a 400 nm thick doped silicon film with doping concentration of 5×10^{21} cm^{-3}.

nanorod emitter can be determined by the relation $\omega_m = \frac{2\pi c}{LRe[n_g]} \cdot m, m = 1,2,3\cdots$, where m denotes the number of the transmission line mode. Here, the tunability associated with the nanorod emitters mainly refers to the resonant frequency tunability, which gives rise to the potential of designing resonance at any given frequency beyond material limitation. With regard to the overall heat flux tunability, the overall heat flux for short nanorod emitters is much lower compared to long nanorod emitters, as shown in Figs. 8(b) and 8(d). This difference results from the decreasing trend of LDOS with increasing angular frequency. For 2 μm long nanorod emitters, the fundamental resonant mode lies in the angular frequency of around 3.5×10^{14} rad/s, where the LDOS is almost one order of magnitude smaller than that for the case of 6 μm long nanorod emitters (around 1.34×10^{14} rad/s), as shown in Fig. 9(a). It should be noted that the corresponding spectral energy density does converge when integrating over the entire angular frequency, as shown in Fig. 9(b).

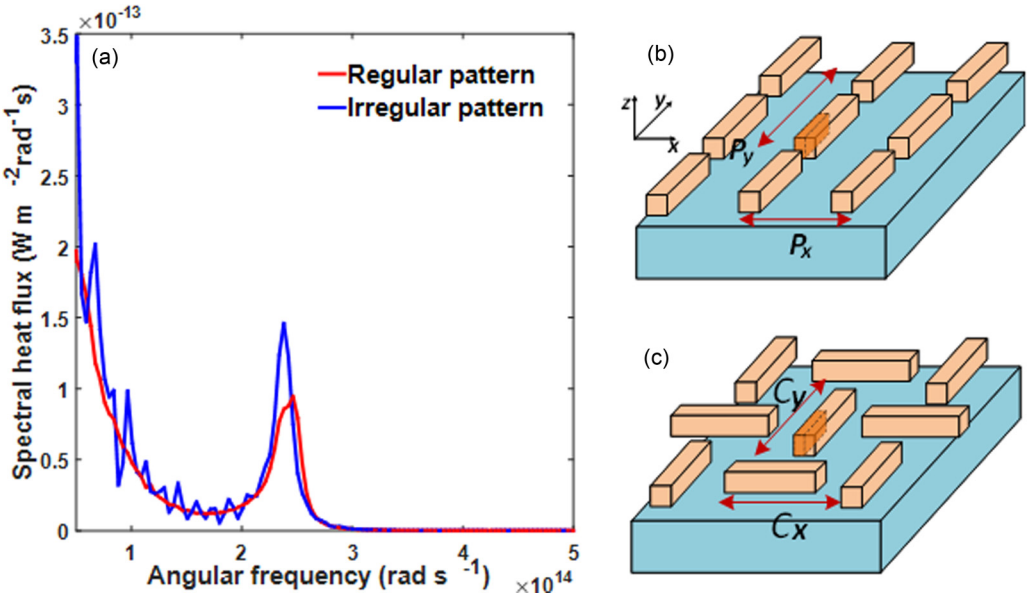

FIG. 10. (a) Radiative heat fluxes for the structures with a layer of patterned finite size nanorod emitters over a thin film, where the red curve represents the radiative heat flux from the nanorods aligned in the y direction, and the blue curve represents the radiative heat flux from unaligned nanorods. Schematics of (b) aligned and (c) unaligned nanorods, where the orange region with a dashed line contour is the WCE unit cell.

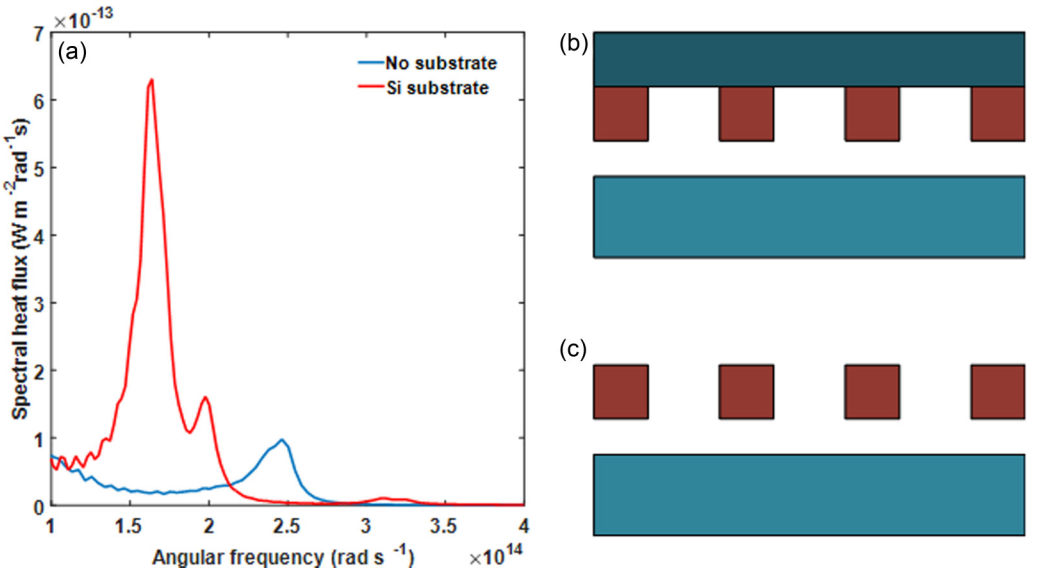

FIG. 11. (a) Radiative heat fluxes for the structures with a layer of patterned finite size nanorod emitters over a thin film, where the blue curve represents the radiative heat flux from the nanorods aligned in the y direction, and the red curve represents the radiative heat flux from the nanorods that are attached to a silicon layer. (b) and (c) Schematics of the nanorods with/without the substrate (dark blue region).

Recall the spectral heat flux between infinitely long nanorod emitters and the thin film absorber plotted in Fig. 7(a). The result shows that while tuning the period along the x direction, there is no correlation between adjacent infinitely long nanorod emitters, which agrees well with the incoherence nature of thermal emission. Such a conclusion still works for the case of finite size nanorod emitters. In Fig. 10, we changed the pattern of the nanorod emitters while simultaneously maintaining the same unit cell area used for the normalization of heat flux, namely $C_x \times C_y = P_x \times P_y$. The length of the each nanorod emitter in the y direction is 3 μm. The simulation result from the WCE formulation shows that the overall heat flux spectra are generally unaffected by the change of the nanorod pattern, which further indicates the spatial incoherence nature of thermal emission. The small fluctuations in the heat flux spectra, in this case, are mainly due to mesh size and calculation error, which can be further optimized. From the perspective of real applications, such finite-size nanorod emitter array could be fabricated on a substrate (e.g., intrinsic silicon) to function as a metasurface. In Fig. 11(a), we calculate the spectral heat flux (red curve) for the case with a silicon substrate attached to the nanorod emitters, where $L_y = 3$ μm. Here the thickness of the silicon substrate is fixed as 100 nm. The frequency redshift and flux intensity increase are clearly observed when comparing the case without the substrate. The redshift of the first resonant frequency is mainly due to the change of effective refractive index n_g. The previously calculated effective refractive index is changed from 1.16 to 1.81, considering the refractive index difference between the nanorod emitter and the silicon substrate. The small bump adjacent to the first peak in the red curve is attributed to a hybrid mode between the emitter and the substrate. As for the increase of the flux peak intensity, the spectral energy density plays a major role since a larger energy density exists for smaller angular frequencies, as shown in Fig. 9(b).

V. CONCLUSION

In this paper, we propose a metamaterial-based structure made from patterned doped silicon nanorods, which exhibits tunable narrow-band thermal emission. The thermal radiation from the metamaterial structure is tuned by designing the Fabry-Pérot cavity mode in a single nanorod. In order to investigate the heat transfer mechanism of the metamaterial structure, we use the WCE formulation as a highly efficient simulation tool to directly calculate the near-field thermal radiation. General principles of the WCE formulation are elucidated, and an algorithm is proposed for calculating symmetric and periodic structures. Implementation of the WCE method with the FDTD method using the DDA is also fully addressed in this paper. The metamaterial structure presented in this paper provides a model for achieving narrow-band thermal emission, which is required for many applications such as infrared sensing and TPVs.

ACKNOWLEDGMENTS

The authors acknowledge funding support from the U.S. National Science Foundation (Grant No. CBET-1253692).

J.L. and B.L. contributed equally to this paper.

[1] S. Basu, Z. M. Zhang, and C. J. Fu, Int. J. Energy Res. **33**, 1203 (2009).

[2] A. Narayanaswamy and G. Chen, Appl. Phys. Lett. **82**, 3544 (2003).

[3] M. Laroche, R. Carminati, and J.-J. Greffet, J. Appl. Phys. **100**, 63704 (2006).
[4] A. Kittel, W. Müller-Hirsch, J. Parisi, S.-A. Biehs, D. Reddig, and M. Holthaus, Phys. Rev. Lett. **95**, 224301 (2005).
[5] Y. De Wilde, F. Formanek, R. Carminati, B. Gralak, P.-A. Lemoine, K. Joulain, J.-P. Mulet, Y. Chen, and J.-J. Greffet, Nature **444**, 740 (2006).
[6] A. C. Jones and M. B. Raschke, Nano Lett. **12**, 1475 (2012).
[7] C. R. Otey, W. T. Lau, and S. Fan, Phys. Rev. Lett. **104**, 154301 (2010).
[8] S. Basu and M. Francoeur, Appl. Phys. Lett. **98**, 113106 (2011).
[9] S.-A. Biehs, F. S. S. Rosa, and P. Ben-Abdallah, Appl. Phys. Lett. **98**, 243102 (2011).
[10] L. Cui, Y. Huang, J. Wang, and K.-Y. Zhu, Appl. Phys. Lett. **102**, 53106 (2013).
[11] P. J. van Zwol, L. Ranno, and J. Chevrier, Phys. Rev. Lett. **108**, 234301 (2012).
[12] B. Guha, C. Otey, C. B. Poitras, S. Fan, and M. Lipson, Nano Lett. **12**, 4546 (2012).
[13] A. Nemilentsau and S. V. Rotkin, Appl. Phys. Lett. **101**, 63115 (2012).
[14] M. Tschikin, S.-A. Biehs, F. S. S. Rosa, and P. Ben-Abdallah, Eur. Phys. J. B **85**, 233 (2012).
[15] K. Joulain, J.-P. Mulet, F. Marquier, R. Carminati, and J.-J. Greffet, Surf. Sci. Rep. **57**, 59 (2005).
[16] A. I. Volokitin and B. N. J. Persson, Rev. Mod. Phys. **79**, 1291 (2007).
[17] V. P. Carey, G. Chen, C. Grigoropoulos, M. Kaviany, and A. Majumdar, Nanoscale Microscale Thermophys. Eng. **12**, 1 (2008).
[18] J.-P. Mulet, K. Joulain, R. Carminati, and J.-J. Greffet, Microscale Thermophys. Eng. **6**, 209 (2002).
[19] E. Rousseau, A. Siria, G. Jourdan, S. Volz, F. Comin, J. Chevrier, and J.-J. Greffet, Nat. Photonics **3**, 514 (2009).
[20] S. Shen, A. Narayanaswamy, and G. Chen, Nano Lett. **9**, 2909 (2009).
[21] L. Hu, A. Narayanaswamy, X. Chen, and G. Chen, Appl. Phys. Lett. **92**, 133106 (2008).
[22] R. S. Ottens, V. Quetschke, S. Wise, A. A. Alemi, R. Lundock, G. Mueller, D. H. Reitze, D. B. Tanner, and B. F. Whiting, Phys. Rev. Lett. **107**, 014301 (2011).
[23] S. Shen, Annu. Rev. Heat Transf. **16**, 327 (2013).
[24] R. St-Gelais, L. Zhu, S. Fan, and M. Lipson, Nat. Nanotechnol. **11**, 515 (2016).
[25] B. Song, Y. Ganjeh, S. Sadat, D. Thompson, A. Fiorino, V. Fernández-Hurtado, J. Feist, F. J. Garcia-Vidal, J. C. Cuevas, P. Reddy, and E. Meyhofer, Nat. Nanotechnol. **10**, 253 (2015).
[26] K. Kim, B. Song, V. Fernández-Hurtado, W. Lee, W. Jeong, L. Cui, D. Thompson, J. Feist, M. T. H. Reid, F. J. García-Vidal, J. C. Cuevas, E. Meyhofer, and P. Reddy, Nature **528**, 387 (2015).
[27] B. Song, D. Thompson, A. Fiorino, Y. Ganjeh, P. Reddy, and E. Meyhofer, Nat. Nanotechnol. **11**, 509 (2016).
[28] T. Kralik, P. Hanzelka, M. Zobac, V. Musilova, T. Fort, and M. Horak, Phys. Rev. Lett. **109**, 224302 (2012).
[29] B. Liu and S. Shen, Phys. Rev. B **87**, 115403 (2013).
[30] S.-A. Biehs, M. Tschikin, and P. Ben-Abdallah, Phys. Rev. Lett. **109**, 104301 (2012).
[31] D. Polder and M. Van Hove, Phys. Rev. B **4**, 3303 (1971).
[32] M. Francoeur, M. P. Mengüç, and R. Vaillon, Appl. Phys. Lett. **93**, 43109 (2008).
[33] A. Narayanaswamy and G. Chen, Phys. Rev. B **77**, 075125 (2008).
[34] C. Otey and S. Fan, Phys. Rev. B **84**, 245431 (2011).
[35] V. A. Golyk, M. Krüger, and M. Kardar, Phys. Rev. E **85**, 046603 (2012).
[36] X. Liu and Z. Zhang, ACS Photonics **2**, 1320 (2015).
[37] R. Guérout, J. Lussange, F. S. S. Rosa, J.-P. Hugonin, D. A. R. Dalvit, J.-J. Greffet, A. Lambrecht, and S. Reynaud, J. Phys. Conf. Ser. **395**, 12154 (2012).
[38] A. W. Rodriguez, M. T. H. Reid, and S. G. Johnson, Phys. Rev. B **88**, 054305 (2013).
[39] A. W. Rodriguez, M. T. Homer Reid, and S. G. Johnson, Phys. Rev. B **86**, 220302(R) (2012).
[40] A. W. Rodriguez, O. Ilic, P. Bermel, I. Celanovic, J. D. Joannopoulos, M. Soljačić, and S. G. Johnson, Phys. Rev. Lett. **107**, 114302 (2011).
[41] S. Edalatpour and M. Francoeur, J. Quant. Spectrosc. Radiat. Transf. **133**, 364 (2014).
[42] R. M. Abraham Ekeroth, A. García-Martín, and J. C. Cuevas, Phys. Rev. B **95**, 235428 (2017).
[43] A. Didari and M. Pinar Mengüç, J. Quant. Spectrosc. Radiat. Transf. **197**, 95 (2017).
[44] A. G. Polimeridis, M. T. H. Reid, W. Jin, S. G. Johnson, J. K. White, and A. W. Rodriguez, Phys. Rev. B **92**, 134202 (2015).
[45] B. Liu, Y. Liu, and S. Shen, Phys. Rev. B **90**, 195411 (2014).
[46] S.-B. Wen, J. Heat Transfer **132**, 72704 (2010).
[47] J.-P. Mulet, K. Joulain, R. Carminati, and J.-J. Greffet, Appl. Phys. Lett. **78**, 2931 (2001).
[48] P. C. Chaumet, A. Rahmani, F. de Fornel, and J.-P. Dufour, Phys. Rev. B **58**, 2310 (1998).
[49] L. Shen and M. K. Chung, in *Third International Symposium on 3D Data Processing, Visualization, and Transmission* (IEEE, Chapel Hill, NC, 2006), pp. 294–301.
[50] P. Ben-Abdallah, K. Joulain, J. Drevillon, and G. Domingues, J. Appl. Phys. **106**, 44306 (2009).
[51] A. I. Volokitin and B. N. J. Persson, Phys. Rev. B **63**, 205404 (2001).
[52] S.-A. Biehs, Eur. Phys. J. B **58**, 423 (2007).
[53] B. Liu, J. Shi, K. Liew, and S. Shen, Opt. Commun. **314**, 57 (2014).
[54] J. Shi, P. Li, B. Liu, and S. Shen, Appl. Phys. Lett. **102**, 183114 (2013).
[55] C. J. Fu and Z. M. Zhang, Int. J. Heat Mass Transf. **49**, 1703 (2006).
[56] B. Liu, J. Li, and S. Shen, ACS Photonics **4**, 1552 (2017).